

THE BIRTH OF MOLECULAR CLOUDS: FORMATION OF ATOMIC PRECURSORS IN COLLIDING FLOWS

FABIAN HEITSCH^{1,2,3}, ADRIANNE D. SLYZ⁴, JULIEN E.G. DEVRIENDT⁴, LEE W. HARTMANN¹, AND ANDREAS BURKERT²

Draft version June 21, 2018

ABSTRACT

Molecular Cloud Complexes (MCCs) are highly structured and “turbulent”. Observational evidence suggests that MCCs are dynamically dominated systems, rather than quasi-equilibrium entities. The observed structure is more likely a consequence of the formation process rather than something that is imprinted after the formation of the MCC. Converging flows provide a natural mechanism to generate MCC structure. We present a detailed numerical analysis of this scenario. Our study addresses the evolution of a MCC from its birth in colliding atomic hydrogen flows up until the point when H₂ may begin to form. A combination of dynamical and thermal instabilities breaks up coherent flows efficiently, seeding the small-scale non-linear density perturbations necessary for local gravitational collapse and thus allowing (close to) instantaneous star formation. Many observed properties of MCCs come as a natural consequence of this formation scenario. Since converging flows are omnipresent in the ISM, we discuss the general applicability of this mechanism, from local star formation regions to galaxy mergers.

Subject headings: turbulence — methods:numerical — ISM:molecular clouds

1. MOTIVATION

Molecular Cloud Complexes (MCCs) in the Galaxy show an abundance of internal structure, both in density and velocity (e.g. Stutzki & Güsten 1990; Falgarone 1990; Mizuno et al. 1995). The density contrasts are non-linear – independent of the importance of gravity (Williams et al. 1995) –, and the MCCs exhibit non-thermal line-widths (Falgarone & Philips 1990; Williams et al. 2000), generally interpreted as supersonic turbulence. Filaments seem to dominate the morphologies in (column) density and velocity (e.g. Bally et al. 1987; Mizuno et al. 1995; Hartmann 2002; Churchwell et al. 2004). The spatial distribution of densities and velocities is consistent with a turbulent spectrum, the details of which are a matter of debate, though (Elmegreen & Scalo 2004).

Extremely puzzling is the source of this wealth of structure. While stellar feedback certainly is a powerful driver (see e.g. Mac Low 2004), it only acts locally, and definitely only after the first stars have formed within the cloud. Moreover, stellar driving might be difficult to reconcile with the observed, nearly self-similar spatial energy distribution.

External drivers suffer from the fact that the cold dense gas essentially acts like a wall to any incoming wave (e.g. Vasquez 1990; Balsara 1996; Elmegreen 1999), preventing an efficient energy transfer from the warm diffuse component to the cold dense phase (see, however, Miesch & Zweibel 1994 for 1D models). Hennebelle & Inutsuka (2005) argue that openings (holes, channels) in a MCC serve as an inroad for Alfvén-waves, however, the question of what forms these chan-

nels remains.

With growing evidence that the lifetimes of molecular clouds – at least in the solar neighborhood – range around a few (2 to 3) Myrs (Elmegreen 2000; Hartmann et al. 2001; Hartmann 2003), a picture in which MCCs are envisaged as transient objects in large-scale atomic colliding flows rather than as well-defined entities in a quasi-equilibrium state (Giant Molecular Cloud, GMC) is emerging. The colliding flows would accumulate atomic gas which might eventually reach column densities high enough for H₂-formation – at which point the “lifetime” of the molecular cloud would start, i.e. the accumulation time could be much longer. Some of the molecular regions might become self-gravitating and form stars instantaneously (Elmegreen 1993, 2000; Ballesteros-Paredes et al. 1999; Hartmann et al. 2001; Pringle et al. 2001; Hartmann 2003). The large-scale flows might be driven by supernova explosions, Galactic shear, or might occur in galaxy interactions (for recent evidence of cloud collisions, see Looney et al. 2006).

We propose and extend the idea (see §2) that the structures observed in MCCs arise from the very processes that form MCCs, i.e. they arise without recourse to non-linear perturbations put in by hand, an approach which defers the problem to an even earlier stage. We investigate numerically the formation of structure in MCC precursors via colliding flows. To avoid the somewhat unwieldy “precursor of Molecular Cloud Complexes”, we will abbreviate this to *PoMCloCs*. By this we mean cold clouds (usually identified as Cold Neutral Medium, CNM), which may be fully atomic or may already contain traces of H₂. In any case, the PoMCloCs serve as the initial stage of Molecular Cloud Complexes, MCCs.

Our numerical models emphasize the ease with which colliding flows generate structure via a combination of dynamical and thermal instabilities. Due to the thermal instability, structure grows predominantly on small scales, leading to early non-linear density perturbations as possible seeds of gravitational collapse and star formation. The resulting line-widths in the cold gas when

¹ Dept. of Astronomy, University of Michigan, 500 Church St., Ann Arbor, MI 48109-1042, U.S.A

² University Observatory Munich, Scheinerstr. 1, 81679 Munich, Germany

³ Dept. of Astronomy, U Wisconsin-Madison, 475 N Charter St, Madison, WI 53706, U.S.A.

⁴ CRAL, Observatoire de Lyon, 9 Avenue Charles André, 69561 St-Genis Laval Cedex, France

seen in projection agree with observed values, however, the cold gas does not seem to exhibit internal supersonic turbulence. Only a few percent of the energy input remains available for driving turbulent motions in the cold gas, the bulk of the energy is lost due to radiative cooling. Within the scope of the models, we find that the time scale for H_2 formation is limited not by a minimum temperature, but by the highly unsteady environment.

This work extends our previous study (Heitsch et al. 2005), in dimensions (here, we present corresponding 3D models), in resolution and in scope of physical applications. Of course, we rely heavily on earlier work (§2). The physics of the problem is described in §3, and the numerical realization as well as numerical artifacts are discussed in §4 and §6.1, in order to provide a background for the interpretation of the results (§5). These are summarized in §6, while §7 suggests possible routes to follow in the future.

2. PREVIOUS AND CURRENT WORK

The concept behind this study is that molecular cloud formation should be seen as a non-equilibrium process. When the perception of the ISM as a dynamical medium gained acceptance, many aspects of molecular cloud and star formation theory were revisited. Hunter (1979) and Hunter & Fleck (1982) re-examined the Jeans criteria and found that converging velocity fields could provoke the gravitational collapse of sub-Jeans mass gas clouds. Tohline et al. (1987) followed this line of thought, further emphasizing that diffuse gas cooling upon compression by even mild velocity and pressure disturbances could easily be transformed to high densities. They applied this idea to externally perturbed spherical clouds. Motivated by these investigations into the role of compressive velocity fields in promoting fast cooling and gravitational collapse, Hunter et al. (1986) used two-dimensional numerical simulations to study the cooling and fragmentation of gas compressed at the interface of two identical, oppositely directed supersonic colliding gas streams.

Since these early works which explored some consequences of a dynamical ISM, molecular cloud formation and evolution has been studied within the framework of compressible turbulence. A strongly fluctuating medium with motions on many scales results in high density albeit transient regions which might be identified as molecular clouds. Large-scale (kiloparsec) models of molecular cloud formation were presented in two-dimensional simulations by Vázquez-Semadeni et al. (1995) and Passot et al. (1995), throwing light on the role of turbulence in the cycle of cloud and star formation (Larson 1981), and specifying conditions for cloud formation in the presence of magnetic fields. But the numerical resolution needed to yield a detailed explanation of the structure and dynamics of molecular clouds makes it necessary to tackle the problem with smaller-scale simulations (tens of parsecs).

For instance, the role played by thermal instability continues to be actively explored. This instability alone has been shown to be an efficient mechanism for generating substructure and even driving turbulence (Burkert & Lin 2000; Kritsuk & Norman 2002a,b, 2004). As indicated by earlier work (e.g. Priest & Heyvaerts 1974 in an application to the solar atmosphere), thermal instability can be triggered by compression. Indeed one-dimensional

plane-parallel simulations of transonic converging flows (Hennebelle & Pérouault 1999, 2000) show how this mechanism transforms inflowing diffuse atomic gas to dense cold gas that is long-lived. Shock waves (driven e.g. by supernova explosions, Mac Low et al. 2005; de Avillez & Breitschwerdt 2005) are another means to create cold, dense gas from warm, diffuse gas. Propagating into the warm ISM, shock waves have been shown to fragment in the presence of thermal instability (Field 1965) and linear perturbations (Koyama & Inutsuka 2000, 2002, 2004b) leading to H_2 -formation within a few Myrs (Bergin et al. 2004). However the passage of a single shock might not leave in its wake enough dense, cold, cloudlets to constitute a MCC. Encounters between streams of transsonically transported gas, on the other hand might be a way to collect, compress, and cool large quantities of gas while at the same time possibly endowing the cold, dense gas with the dynamical and structural characteristics of molecular cloud complexes. This scenario has recently come into the spotlight.

In high-resolution two-dimensional simulations of supersonic, colliding gas flows, Audit & Hennebelle (2005) confirm that even in a very dynamical environment a bistable medium develops as compressions initiate thermal instability. However their study concentrates on how turbulence generates and influences thermally unstable gas, not on the reverse problem of how thermal instability could feed the turbulence characteristic of molecular clouds. In three-dimensional simulations of transonic colliding flows, Vázquez-Semadeni et al. (2006) show that a thin cold sheet, reminiscent of those observed by Heiles & Troland (2003) and Heiles (2004) forms at the junction of the two flows. It develops turbulence which they attribute to the Non-linear Thin Shell Instability (NTSI, Vishniac 1994). Furthermore they find that even in simulations without gravity, the highest density gas is overpressured with respect to the mean warm neutral medium pressure, suggesting that the ram pressure of the colliding flows is responsible.

To be fair, we should mention that favorable conditions for molecular cloud formation not only exist in converging flows, but also in “focal planes” of (sustained) MHD-waves, as Elmegreen (1999) shows. However, he notes that while highly structured MCCs form in such a system, the cold gas does not acquire significant turbulence.

The notion of generating the turbulent substructure of molecular clouds by their formation process has been discussed in various contexts (e.g. Ballesteros-Paredes et al. 1999; Hartmann et al. 2001; Audit & Hennebelle 2005; Vázquez-Semadeni et al. 2006). Audit & Hennebelle (2005) emphasized the evolution of the thermal states in the colliding flows, and provided a semi-analytical model for the evolution of a gas parcel. One of the main differences to the present study is that they impose velocity perturbations on their incoming gas flow – as do Vázquez-Semadeni et al. (2006), although as “random noise” at a percent-level –, whereas we defer the structure generation to the actual flow collision site. Vázquez-Semadeni et al. (2006) compared in detail analytical solutions with one-dimensional and three-dimensional models. Koyama & Inutsuka (2002) and their subsequent work discuss molecular cloud formation behind a shock-compressed layer, more resembling the situation of an expanding shell. In their case, the initial

perturbations reside in the density field. The present study extends the “proof of concept” of “structure formation from scratch” in two dimensions presented in Heitsch et al. (2005) by focusing on the dynamical state and the turbulent properties of the PoMCloC during its formation, and on the conditions necessary for the onset of H₂ formation.

3. PHYSICS

We restrict the models to hydrodynamics with radiative cooling, leaving out the effects of gravity and magnetic fields. Gravity would lead to further fragmentation, and magnetic fields could have a stabilizing effect (see also discussion in §7). For this regime, then, we identify three relevant instabilities, namely the NTSI, the Kelvin-Helmholtz-Instability (KHI) and the Thermal Instability (TI). This enumeration of course does not mean that the instabilities work independently of each other. Rather, the resulting dynamical system is a consequence of a combination of all three instabilities, however, in degrees depending on the local flow properties.

3.1. NTSI

The NTSI (Vishniac 1994, Fig. 1) arises in a shock-bounded slab, when ripples in a two-dimensional slab focus incoming shocked material and produce density fluctuations. Gas streaming along the x -direction will be deflected at perturbation peaks and collect in the troughs. Thus, x -momentum is transported laterally (along the y -direction). For a weak equation of state, the slab can act as a wall to deflect the incoming gas streams, while for an adiabatic one, the bounding shocks will travel faster at the y -locations of the troughs because of the higher compression, thus leveling out the initial perturbations (see Vázquez-Semadeni et al. (2006) for a discussion of the speed of the bounding shock). The growth rate is $\sim c_s k(k\Delta)^{1/2}$, where c_s is the sound speed, k is the wave number along the slab, and Δ is the amplitude of the spatial perturbation of the slab.

Various aspects of the NTSI have been investigated numerically. Hunter et al. (1986) and Hueckstaedt (2003) focused on the combination of the NTSI and self-gravity. The former authors found a criterion for forming self-gravitating fragments either under isothermal conditions or with line-cooling. Hueckstaedt (2003) discussed the effect of the cooling strength on the evolution of the NTSI, stating that strong cooling leads to small-scale fragmentation which wipes out the NTSI-effects. Blondin & Marks (1996) investigated Vishniac’s analysis numerically, noting that the shear flows along the slab lead to Kelvin-Helmholtz modes and identifying them as the main cause for the internal structure of the slab. Although in their radiative shock study, Walder & Folini (1998) focused mainly on the interaction of stellar winds, they extended the argument and the implications to the more general interstellar medium (Walder & Folini 2000). Klein & Woods (1998) studied the NTSI in the context of cloud collisions, applying the process to the formation of clumpy filaments in e.g. the Orion Molecular Cloud. They partially included magnetic fields, following the magnetic pressure term and the induction equation, but leaving out the tension term of the Lorentz-force.

3.2. KHI

The flows deflected at the slab (as indicated in Fig. 1) can cause shear instability modes, which have been studied at great length (e.g. Chandrasekhar 1961; Sen 1964; Gerwin 1968; Roberts 1974; Ferrari & Trussoni 1983; Sandham & Reynolds 1991; Keppens et al. 1999; Malagoli et al. 1996, to name a few). In the incompressible case, for a step function profile in the velocity and constant densities across the shear layer, the growth rate is given by the velocity difference $k\Delta U$, i.e. all wave modes get unstable. If aligned with the flow, magnetic fields can stabilize against the KHI via the tension component of the Lorentz force, and the growth rate is given by $k\sqrt{\Delta U^2 - c_A^2}$, i.e the modes that will get unstable are those for which the flow velocity difference is larger than the Alfvén speed c_A . For compressible gas, the situation changes substantially: the system will be stable for all those wave numbers whose effective Mach number is larger than a critical value (Gerwin 1968). Thus, while Kelvin-Helmholtz modes definitely *will* play a role in the suggested scenario, Figure 1 certainly can give only a very simplified picture.

3.3. TI

The TI (Field 1965) rests on the balancing of heating and cooling processes in the ISM. The TI develops an isobaric condensation mode and an acoustic mode, which – under ISM-conditions – is mostly damped. The condensation mode’s growth rate is independent of the wave length, however, since it is an isobaric mode, smaller perturbations will grow first (Burkert & Lin 2000). Heat conduction sets the smallest growth scale. If this scale is not resolved numerically, perturbations will grow at the resolution scale (Koyama & Inutsuka 2004a). The signatures of the TI are fragmentation and clumping. They persist as long as the sound crossing time across a density perturbation is smaller than the cooling time scale

$$|\tau_c| \equiv \frac{3}{2} \frac{kT}{|\Gamma - n\Lambda|}. \quad (1)$$

The TI can drive turbulence in an otherwise quiescent medium, even continuously, if an episodic heating source is available (Kritsuk & Norman 2002a,b).

4. NUMERICS

All three instabilities grow fastest or at least first on the smallest scales. This poses a dire challenge for the numerical method. We chose a method based on the 2nd order Bhatnagar-Gross-Krook formalism (Prendergast & Xu 1993; Slyz & Prendergast 1999; Heitsch et al. 2004; Slyz et al. 2005), allowing control of viscosity and heat conduction. The code evolves the Navier-Stokes equations in their conservative form to second order in time and space. The hydrodynamical quantities are updated in time unsplit form. As shown below, statistical properties of the models are resolved with respect to grid resolution, viscosity and heat conduction, although the flow patterns change in detail — as is expected in a turbulent environment.

4.1. Heating and Cooling

The heating and cooling rates are restricted to optically thin atomic lines following Wolfire et al. (1995),

so that we are able to study the precursors of MCCs up to the point when they could form H_2 . Dust extinction becomes important above column densities of $N(\text{HI}) \approx 1.2 \times 10^{21} \text{cm}^{-2}$, which are reached only in the densest regions modeled. Thus, we use the unattenuated UV radiation field for grain heating (Wolfire et al. 1995), expecting substantial uncertainties in cooling rates only for the densest regions. The ionization degree is derived from a balance between ionization by cosmic rays and recombination, assuming that Ly α photons are directly reabsorbed. Numerically, heating and cooling is implemented iteratively as a source term for the internal energy e of the form

$$\partial_t e = n\Gamma(T) - n^2\Lambda(T) \quad (2)$$

in units of energy per volume per second. Here, Γ is the heating contribution (mainly photo-electric heating from grains), $n\Lambda$ the cooling contribution (mainly due to the CII HFS line at $158\mu\text{m}$). Since the cooling and heating prescription has to be added outside the flux computations, it lowers the time order of the scheme. To speed up the calculations, equation (2) is tabulated on a 2048^2 grid in density and temperature. For each cell and iteration, the actual energy change is then bilinearly interpolated from this grid.

4.2. Initial and Boundary Conditions

Two opposing, uniform, identical flows in the x - y computational plane initially collide head-on at a sinusoidal interface with wave number $k_y = 1$ (and $k_z = 1$ for 3D models) and amplitude Δ (Fig. 1). The incoming flows are in thermal equilibrium. The system is thermally unstable for densities $1 \lesssim n \lesssim 10 \text{cm}^{-3}$. The cooling curve covers a density range of $10^{-2} \leq n \leq 10^3 \text{cm}^{-3}$ and a temperature range of $30 \leq T \leq 1.8 \times 10^4 \text{K}$. The box side length is 44pc. Thus, Coriolis forces from Galactic rotation are negligible, however, the simulation domain is large enough to accommodate a moderately-sized molecular cloud complex. For an interface with $\Delta = 0$, a cold high-density slab devoid of inner structure forms. The onset of the dynamical instabilities thus can be controlled by varying the amplitude of the interface perturbation. This allows us to test turbulence generation under minimally favorable conditions. This setup might seem artificial: (1) The incoming flows are not expected to be perfectly uniform, however, we chose to defer the moment of structure generation to the last possible moment in the simulation, instead of imposing perturbations on the incoming flows (see §4.4.3). (2) As we will see below, the model run times extend considerably beyond 10Myrs. At an inflow speed of 10km s^{-1} this would correspond to a total extent of the system of 200pc. This suggests that the initial densities of the flows are more likely to be a few cm^{-3} to form molecular clouds with flows of order 50-100 pc length. Spiral density waves can also produce coherent flows of the length required, at least in principle.

The boundary conditions in the transverse (i.e. y and z) directions are periodic, while in the x -direction, the boundary values are defined as uniform inflow at constant density n_0 and inflow speed v_0 . Consequently, the boundaries cannot treat outgoing waves or flows. Thus, the models have to be halted once the bounding shocks reach the boundaries. The corresponding time scales have been discussed by Vázquez-Semadeni et al. (2006).

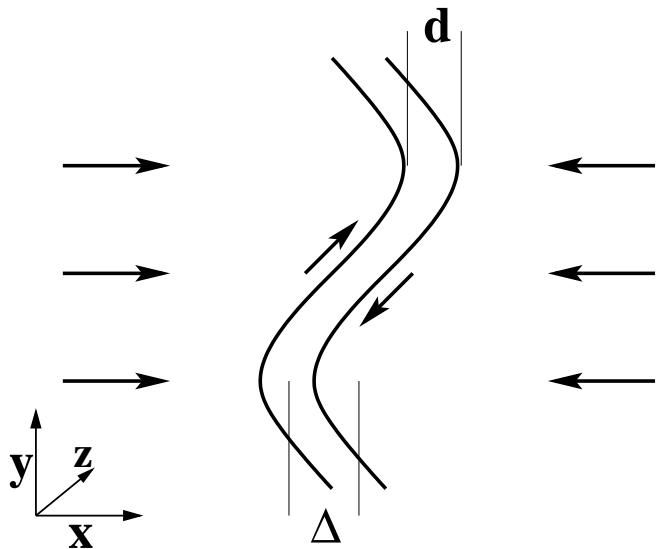


FIG. 1.— Sketch of the NTSI mechanism and geometry of the initial conditions. Gas is streaming along the x -direction and colliding at the perturbed interface. The resulting shear flows excite KH-modes.

To facilitate the analysis of the dynamics and time history of the cold gas, the code is equipped with Lagrangian tracer particles, that are advected after each flux update. Tracer particles are deployed at grid cell centers where $T < 300\text{K}$ and in four generations, starting at approximately 5 Myrs in intervals of 2.5 Myrs. This allows us to study the effect of turbulent motions on the fluid parcels as well as the time history of (representative) regions of cold gas. Extending the model sequence of Heitsch et al. (2005), we varied the parameters, dimensions and resolution of the models (see Table 1).

Before we discuss the simulation results and their physical implications, we assess the numerical reliability of the code for the problem at hand. We will restrict the numerical discussion to the 2D models, since similar effects pertain to the 3D models.

4.3. Asymmetries

Figure 2 shows stills of models 2C10c, 2C20c and 2C30c (i.e. a sequence in Mach numbers 1, 2 and 3) taken 11.5 Myrs after flow contact time. While model 2C10c preserves the symmetry of the initial conditions, at larger Mach numbers, the structures develop strong asymmetrical features with respect to the mid-plane.

Since this could be cause for concern, we measured the degree of asymmetry in the models with time (Fig. 3). Asymmetry is defined in terms of the density differences as

$$A = \left\langle \left(\frac{\Delta n}{n} \right)^2 \right\rangle^{1/2}, \quad (3)$$

where the average is over all cells with $\Delta n > 0$ (and not over the whole domain in order to exclude the inflow initial conditions which are symmetric), and Δn is the absolute value of the density difference between cells which should be symmetric across the upper and lower half of the simulation midplane. The initial conditions are perfectly symmetric, but slight differences at the machine accuracy level in the reconstruction of hydrodynamical

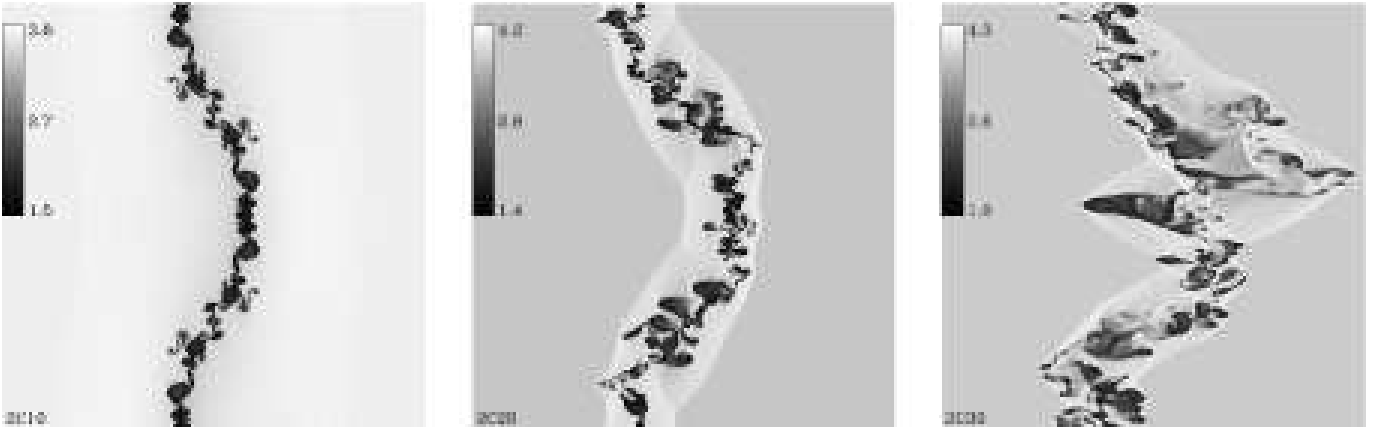


FIG. 2.— Logarithmic temperature maps of the two-dimensional models 2C10c, 2C20c and 2C30c, i.e. with inflow speeds at Mach 1, 2 and 3. The temperature range is given in $\log T$ [K]. The stills are taken approximately 11.5 Myrs after flow contact.

TABLE 1. MODEL PARAMETERS

run	N	\mathcal{M}_0	v_0 [km s $^{-1}$]	T_0 [K]	n_0 [cm $^{-3}$]
2B10	b,c	1.0	5.3	2.5×10^3	1.0
2B20	b,c	2.0	10.6	2.5×10^3	1.0
2B30	b,c	3.0	15.9	2.5×10^3	1.0
2C10	b,c	1.0	8.9	5.3×10^3	0.5
2C15	b	1.5	13.4	5.3×10^3	0.5
2C20	b,c,d	2.0	17.8	5.3×10^3	0.5
s/12C20	b	2.0	17.8	5.3×10^3	0.5
2C25	b	2.5	22.4	5.3×10^3	0.5
2C30	b,c,d	3.0	26.7	5.3×10^3	0.5
s/12C30	b	3.0	26.7	5.3×10^3	0.5
2C35	b	3.5	31.2	5.3×10^3	0.5
3C10	a	1.0	8.9	5.3×10^3	0.5
3C20	a	2.0	17.8	5.3×10^3	0.5
3C30	a	3.0	26.7	5.3×10^3	0.5

Note. — The first column lists the runs. The first digit of the model name stands for the dimension of the simulation, the second denotes the atomic particle density in the warm medium (where B corresponds to $n_0 = 1$ cm $^{-3}$ and C corresponds to $n_0 = 0.5$ cm $^{-3}$ as indicated in the column marked n_0), and the third and fourth digits indicate the Mach number of the inflow. The second column lists the linear resolution N of the simulation where the letters a , b , c and d correspond to 256, 512, 1024 and 2048 grid cells per simulation box side. Where there is more than one letter, it means that more than one simulation was run (and not that the box size is oblong). The subsequent columns list the inflow Mach number \mathcal{M}_0 , inflow velocity v_0 , initial temperature T_0 and density n_0 . The models s/12C20 and s/12C30 are discussed in §6.1.

variables eventually lead to a difference in the cooling strength and thus cause perceptible asymmetries. The code preserves perfect symmetry for a purely adiabatic equation of state (i.e. without the additional heating and cooling terms). After onset, the asymmetries grow linearly in time until they reach a saturation level between $A \approx 50$ and 100. This corresponds approximately to the temperature (and density) contrast between the warm and cold gas and thus to the maximum asymmetry reachable for the system. Although the asymmetries increase with Mach number and – to a lesser extent – with resolution, they only appear well after the system has evolved. Koyama & Inutsuka (2002), Audit & Hennebelle (2005) and Vázquez-Semadeni et al. (2006) chose an alternative route: they added perturbations (in density or velocity)

to the incoming flow, thus breaking the symmetry of the initial conditions. While the physical reason for adding perturbations to the inflow is perfectly obvious, in the present study we want to emphasize the point that even with the least possible perturbation to the flow, (turbulent) substructures are generated with ease. In some sense, this is an attempt to carry the argument to extremes.

Conversely, one could argue that imposing perturbations on the incoming flow helps to hide the symmetry breaking due to truncation errors. To get a stronger handle on how our somewhat extreme initial conditions are affecting the results, we repeated model 2C20 twice, once with an interface perturbation mode of $k_y = 32$ instead of $k_y = 1$, and in the second repetition with the $k_y = 32$ -mode overlaid on the $k_y = 1$ mode at $(1/32)^{5/3}\%$ of the amplitude at $k_y = 1$, motivated by a turbulent cascade. In both cases, the system develops small-scale structures at $k_y = 32$, meaning that the instability grows at the smallest imposed ($k_y = 32$) scales, as long as these are larger than the Field length (see next section).

4.4. Heat Conduction

Koyama & Inutsuka (2004a) demonstrated with 1D models that the choice of the heat conductivity κ can strongly influence the dynamics of the system. Especially they argue that a too low heat conductivity can damp turbulent motions in the cold phase and can lead to artificial fragmentation at the grid scale (see however Vázquez-Semadeni et al. 2006). The critical parameter here is the Field length (Field 1965) – the length scale below which heat conduction can stabilize the TI –

$$\lambda_F \equiv \left(\frac{\kappa T}{n^2 \Lambda} \right)^{1/2} \quad (4)$$

where κ is the heat conductivity (see below), and Λ is the cooling function from equation (2). With a heat conduction of $\kappa = 2.5 \times 10^3 (T/[K])^{1/2}$ (Parker 1953), Koyama & Inutsuka (2004a) conclude that for ISM-conditions, a linear resolution of several thousand cells is needed (they get convergence at 16384 cells).

The heat conduction in the BGK scheme can be controlled explicitly (see Slyz et al. 2006 for an analysis) by varying the kinematic viscosity, since the Prandtl number in the code is $Pr \equiv 1$ by construction. The choice of

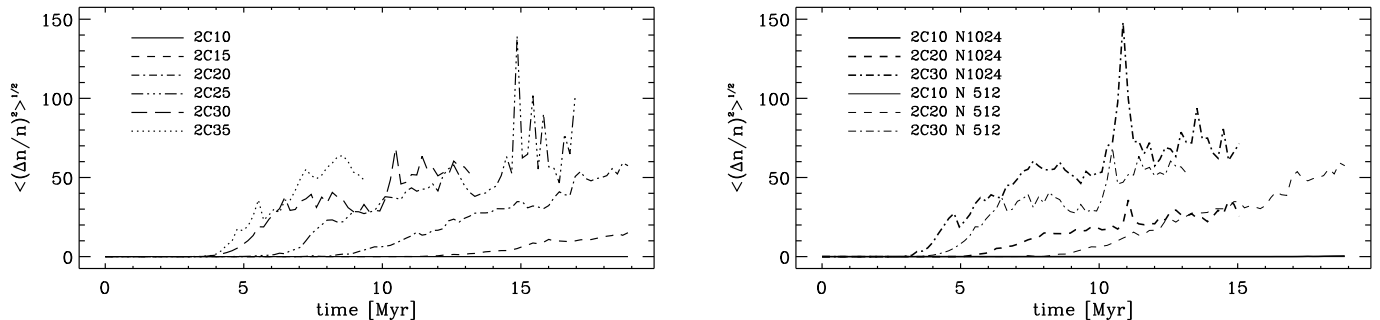


FIG. 3.— *Left*: Asymmetry around midplane $y = 0$ against time for model sequence 2C at the six available Mach numbers for resolution $N = 512$. *Right*: Asymmetry around midplane $y = 0$ against time for model sequence 2C at resolutions $N = 512$ and $N = 1024$.

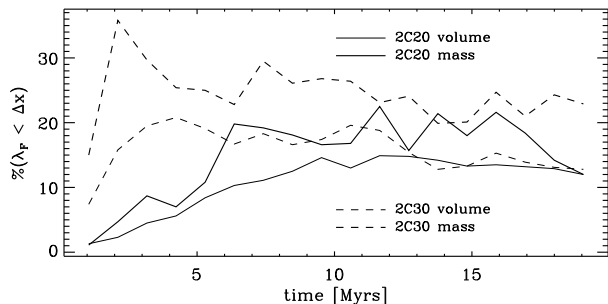


FIG. 4.— Volume and mass fraction of Field-unresolved cells (eq. [4]) in the cold gas (other temperature regimes are not affected) against time for runs with resolution $N = 512$ ($\Delta x = 0.34\text{pc}$).

the viscosity is controlled by two considerations, namely (a) it should be large enough to prevent numerical artifacts on small scales, and (b) it should be small enough to leave enough dynamical range. Obviously, both requirements are difficult to meet simultaneously.

To establish to what degree our models are resolved, we begin by measuring the Field lengths (eq. [4]) cell-wise, excluding all cells which belong to the inflow, since their thermal time scale $\tau_c \rightarrow \infty$. Figure 4 shows the volume and mass fractions of the Field-unresolved cells against time for models 2C20c and 2C30c. Note that when the volume and mass fractions agree, the bulk of the non-equilibrium gas is in the cold phase (see also Fig. 16). In other words, Figure 4 and the following ones refer (mostly) to the cold gas phase. Thus, between 10% and 20% of the volume, and between 10% and up to 30% of the mass of the cold gas are not resolved. This is acceptable as long as we devise a selection criterion for the subsequent analysis.

Figure 5 lets us estimate the size of the smallest structures we can resolve. Again, we distinguish between volume and mass fractions, which however in this case are close to identical. The figure indicates that the Field length for the bulk of the mass and volume lies between 1 and 32 pc, scales which are well resolved by all our models. For our lowest resolution 2D runs ($N = 512$), the resolution limit is $\Delta x = 0.34\text{pc}$. Thus, for the subsequent discussions, we will only consider structures with sizes larger than 0.34pc for 2D runs, and 0.68pc for 3D runs.

If the Field-length is not resolved, structures tend to grow on grid scales, i.e with increasing resolution, there

should be more and more small-scale structures. This effect is clearly visible in the left panel of Figure 6, which shows a histogram of the size of cold regions ($T < 300\text{K}$). The size of a cold region is defined as the geometric mean of its minimum and maximum diameter. The inset numbers give the average number of cold regions per line of sight, i.e. normalized to resolution. If the Field length were resolved, heat conduction would lead to a cutoff at small L_{cold} . Selecting for regions with $L_{\text{cold}} > 0.34\text{pc}$, the histograms (and the average number of cold regions) agree sufficiently to proceed with the above selection criterion.

5. RESULTS

5.1. Turbulence

Molecular Clouds consistently show non-thermal line-widths of a few km s^{-1} (e.g. Falgarone & Philips 1990; Williams et al. 2000) that – together with temperatures of $T \approx 10\text{K}$ – are generally interpreted as supersonic turbulence. The line-widths in our models are consistent with the observed values (Fig. 7). The broad line wings are non-Gaussian. This may be a sign of intermittency (e.g. Falgarone & Phillips 1996; Lis et al. 1996).

The "observed" linewidth is derived from the histogram of the density-weighted line-of-sight velocity dispersion in the cold gas at $T < 300\text{K}$ (Fig. 8, filled symbols). This linewidth would correspond to linewidths in the cold neutral medium as e.g. traced by HI. Since the *internal* line-widths of coherent cold regions (open symbols) range around the sound speed of the cold gas (0.7km s^{-1}), the *internal* velocity dispersions do not reach Mach numbers $\mathcal{M} > 1$ (see also Koyama & Inutsuka 2002; Audit & Hennebelle 2005). Hence, the "supersonic" line-widths are a consequence of cold regions moving with respect to each other within a warmer and more diffuse medium, but not a result of internal supersonic turbulence in the cold gas which eventually would be hosting star formation (Hartmann et al. 2001; Kwan & Sanders 1986). Note from Figure 9, that this result is independent of resolution and geometry. Because of the thermal instability, to make figure 8 and 9 cold coherent regions are identified via a temperature threshold at $T < 300\text{K}$. Figure 10 shows the temperature distribution according to volume and mass for models 2C20 and 2C30 (at $N = 1024$). Note that the above temperature criterion identifies the bulk of the cold gas. The choice of $T = 300\text{K}$ as a "defining" temperature for the PoMCloCs is motivated by Figure 10. Although the

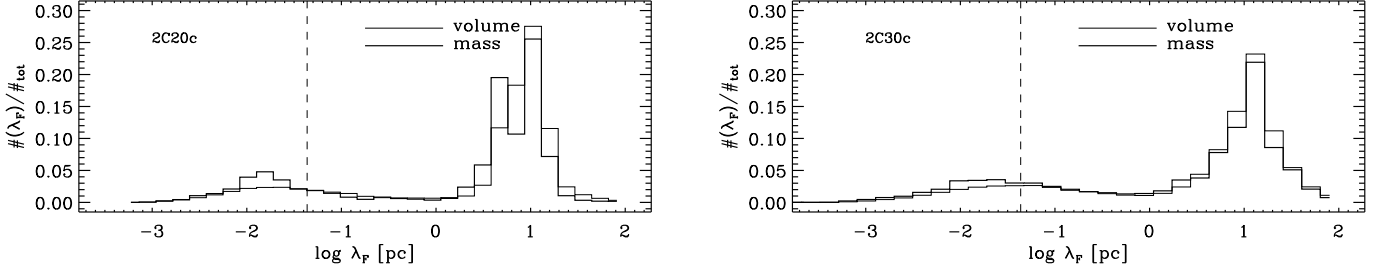


FIG. 5.— Histograms of the Field lengths (eq. [4]) for models 2C20c (left) and 2C30c (right) 12 Myrs after flow contact. The vertical dashed line denotes the resolution limit for $N = 1024$.

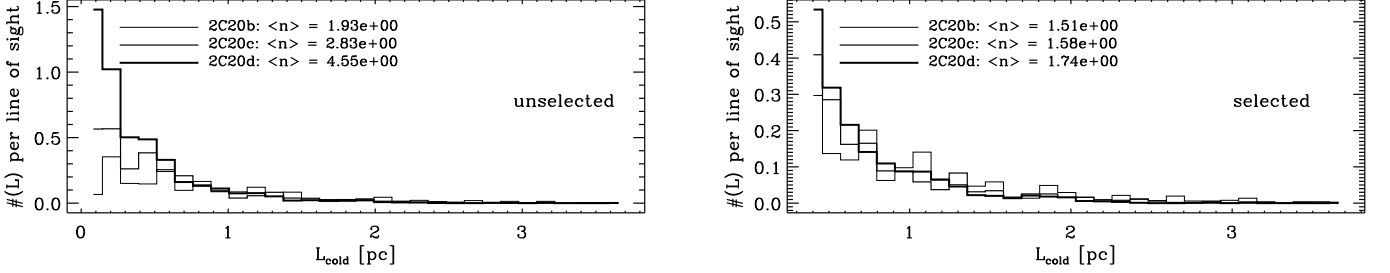


FIG. 6.— Histograms of the size of cold regions ($T < 300\text{K}$) per line of sight, i.e. normalized to resolution for models 2C20b, c, and d. The inset numbers give the average number of cold regions per line of sight. *Left*: All regions (down to the size of 1 cell) have been considered. There is a clear trend to larger numbers with increasing resolution. *Right*: Same histogram but selected for regions with $L_{\text{cold}} > 0.34\text{pc}$.

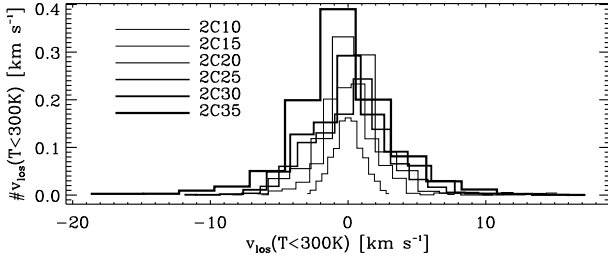


FIG. 7.— Histogram of the “observed” line-of-sight velocity dispersion in the cold gas ($T < 300\text{K}$) for a model sequence in Mach numbers, 12 Myrs after initial flow contact. Shown are models at $N = 512$. Line-of-sight velocity dispersions are determined along the inflow direction (x -axis, see Fig. 1), and then laterally averaged. Observed velocity dispersion values are reached easily. See text for the choice of $T = 300\text{K}$ as “defining” temperature for the PoMClOcs.

histogram does not include gas at the inflow temperature, the volume is dominated by warm gas ($T \sim 10^{3.9}\text{K}$), while the mass is dominated by cold gas ($T \sim 40\text{K}$). The variations of the line-of-sight velocity dispersion with time is within the error bars shown.

Are the line-widths actually indicating turbulent motions, or are we seeing the inflow motions of (already) cold gas (e.g. Vázquez-Semadeni et al. 2006)? If the gas motions are truly turbulent, the average Lyapunov exponents

$$\langle \Lambda \rangle \equiv \left\langle \frac{1}{t - t_0} \log \frac{d(t)}{d(t_0)} \right\rangle \quad (5)$$

should be positive, indicating a growing separation between neighboring particles. In equation (5), t_0 is the start time of particle advection, and d are the corresponding separations of neighboring particles. The average refers to the simulation domain. After an initial

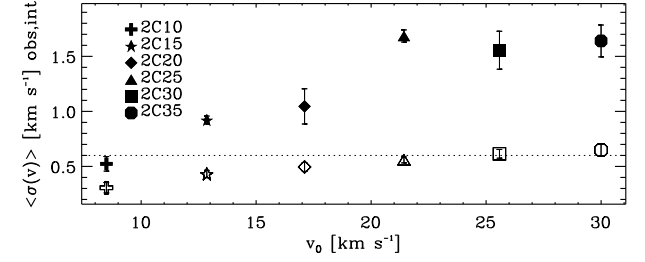


FIG. 8.— “Observed” (filled symbols) and internal (open symbols) velocity dispersion in the cold gas ($T < 300\text{K}$) against inflow speed for the same sequence of models as in Figure 7, 12 Myrs after initial flow contact. Resolution is $N = 512$. The dashed line denotes the sound speed in the cold gas. The internal velocity dispersion reaches Mach 1 at most.

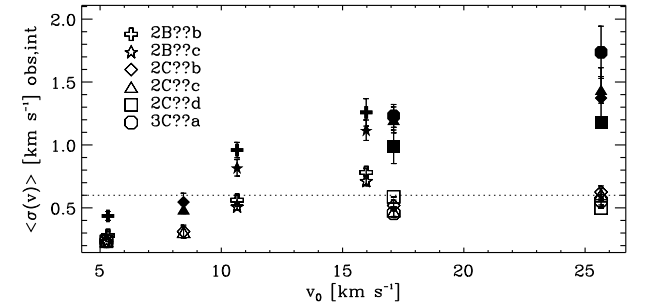


FIG. 9.— “Observed” (filled symbols) and internal (open symbols) velocity dispersion in the cold gas ($T < 300\text{K}$) for a selection of models against inflow speed, 12 Myrs after initial flow contact. Question marks in the model names are wild cards for the Mach number. The dashed line denotes the sound speed in the cold gas.

compression phase with $\langle \Lambda \rangle < 0$, the cold gas becomes

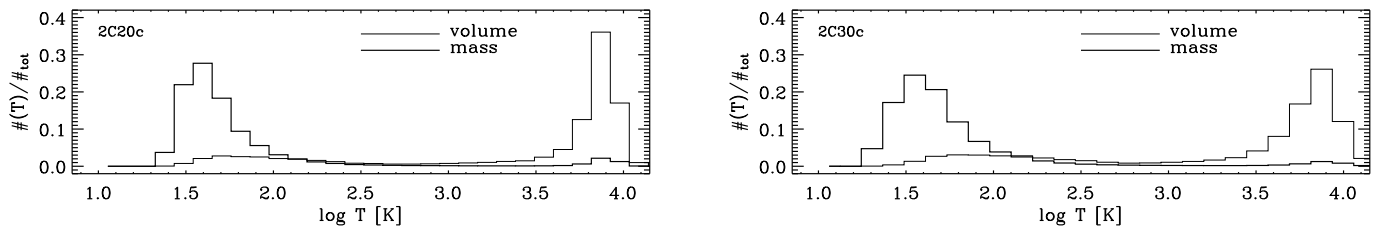


FIG. 10.— Histogram of temperature for models 2C20 (left) and 2C30 (right) at $N = 1024$, and 12 Myrs after flow contact. The cold gas dominates the mass (thick lines), while the warm gas dominates the volume (thin lines).

turbulent (Fig. 11). With higher Mach number, the onset of internal turbulence in the slab is delayed, which is mirrored by the lower Lyapunov exponents. Higher resolution leads to larger $\langle \Lambda \rangle$ at the time of the onset of turbulence, which is defined as $t(\langle \Lambda \rangle > 0)$. For $N = 1024$, the initial separation of tracer particles is smaller, so that a larger spatial range can be covered. All exponents are positive, independent of resolution, and converge for late times.

The power spectrum of the specific kinetic energy v^2 (Fig. 12 for model 3C20) can be used as another diagnostic of turbulence in the models. Shown are the three linear spectra, taken along the inflow direction (α_x) and the transversal directions ($\alpha_{y,z}$). The spectral index $\alpha_x = -1.96$ is consistent with the Fourier transform of a step function, as to be expected since the strong decelerations along the x -direction effectively lead to a discontinuity in v^2 (Note that for the initial conditions, not v^2 but v is discontinuous.). The spectral indices in the transversal directions, α_y and α_z , are consistent with a Kolmogorov spectrum, indicating fully developed turbulence. The lower spectrum (denoted by triangles and a corresponding slope $\alpha_c = -3.24$) shows the spectrum averaged over spheres of constant wavenumber k . Error bars denote errors on the mean. Within the errors, the slope is still consistent with a Kolmogorov spectrum of $-11/3$ in three dimensions. The last half decade is dominated by numerical diffusion, leaving us approximately 1.5 decades for physical analysis.

The spectral indices differ depending on whether the spectrum is taken along the inflow or transversally. Another way to see this is to split the specific kinetic energy into a compressible (and translational) part with $\nabla \times \mathbf{v} \equiv 0$ and a solenoidal part with $\nabla \cdot \mathbf{v} \equiv 0$. For the full domain (models 2C20 and 3C20), the specific kinetic energy is clearly dominated by the compressible part, because of the inflows (Fig. 13, *left*). Note however, that the solenoidal part (thin lines) is steadily increasing. Even though the energy input rate is constant, the total specific kinetic energy (thick lines) decays with time as a consequence of the radiative cooling (see below). The specific energy restricted to the cold gas (at $T < 300\text{K}$, Fig. 13, *right*) is dominated by the solenoidal component, and all components increase with time, indicating that once the gas has cooled down to its minimum temperature, it starts to store the kinetic energy from the inflows. The solenoidal components are slightly larger for the 3D models, which is not surprising since the extra degree of freedom allows the gas to evade compression more efficiently.

One might speculate as to whether the total specific

kinetic energy will decrease until it has reached a minimum at the moment when (most of) the gas has cooled down to the minimum temperature given by the cooling curve, or whether it does find some kind of equilibrium between kinetic energy input and thermal energy loss. Since with increasing density, the cooling will get more and more efficient, the latter seems unlikely. However, it is probably even more unlikely that the inflows are maintained for times long enough to establish equilibrium between kinetic energy input and thermal energy loss. Moreover, once gravity dominates the cold, dense regions, rather than reach a state of equilibrium, the clouds might pass through the phases of initial compression, turbulence generation, cooling and finally gravitational collapse.

5.2. Thermal states

Structure forms in colliding flows as a result of an interplay between dynamical and thermal instabilities. The dynamical instabilities generate compressions and shear flows, while the thermal instabilities amplify density perturbations to the non-linear regime where they become potential seeds for self-gravitating structures. The effect of the TI on the thermal state of the gas is shown in Figure 14.

The solid line denotes the $P(n)$ relation in thermal equilibrium. It is a direct result of the heating and cooling processes included and displays the usual three regimes, namely an “atomic” regime for $\log n < -0.5$ with an effective $\gamma_e \approx 5/3$, an “isothermal” regime for $\log n > 1.5$ with $\gamma_e \rightarrow 1$, and an unstable regime with $\gamma_e < 0$.

Each cell in the scatterplots Figures 14 and 15 is color-coded with its thermal time scale (eq. [1]). Positive time scales denote heating (towards red colors) and negative time scales correspond to cooling (towards blue colors). At high densities, the thermal time scales are short (greenish colors), which is mirrored in the very small scatter in $\log P$ around the equilibrium curve. Moving to lower densities, the cooling time scale increases dramatically, until we reach the instability regime, which consists of a black triangular region in $P(n)$. This consists mostly of gas which has passed the bounding shocks (slightly increased densities due to the (nearly) adiabatic shock), but has not yet reached the cold dense phase. Since there is no gravity in the simulation, the ram pressure of the inflow (see dashed lines in Fig. 14) limits the maximum pressure gas can reach in the system, apart from slight overshoots due to waves. A substantial amount of gas resides at higher pressure than that of the ambient inflow (higher by a factor of approximately 6 for model 2C20, and by 13 for model 2C30). This gas has been “overpres-

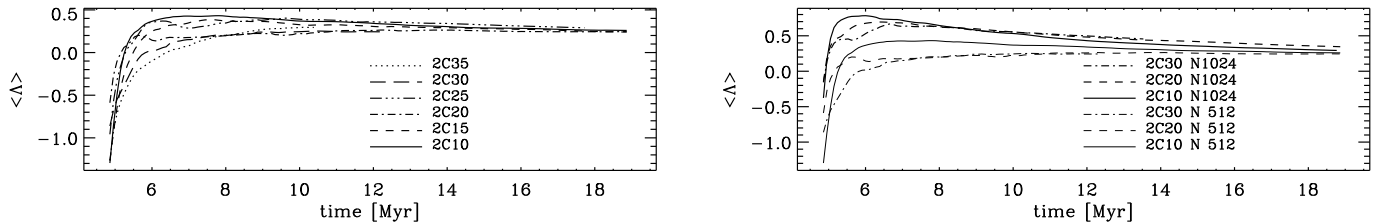


FIG. 11.— *Left*: Average Lyapunov exponents (eq. [5]) for a sequence of models in Mach number against time. After the initial compression phase, the cold gas becomes turbulent. Only the first tracer particle generation is used. Models shown in this diagram were run at $N = 512$. *Right*: Resolution effects. Higher resolution leads to larger $\langle \Lambda \rangle$, although all $\langle \Lambda \rangle > 0$.

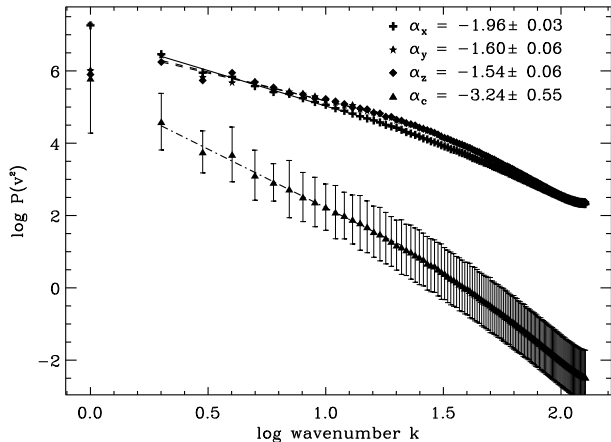


FIG. 12.— Specific kinetic energy spectrum for model 3C20 at 15 Myrs. The linear spectral indices $\alpha_{x,y,z}$ refer to the coordinate directions, and α_c gives the index of the spherically averaged spectrum. Along the inflow, the strong decelerations effectively lead to a step function in $\langle v^2 \rangle$, mirrored in the steeper index. Due to numerical dissipation, the last half decade is not available for physical analysis.

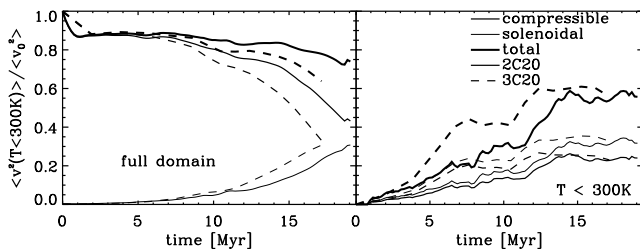


FIG. 13.— *Left*: Specific kinetic energy for the whole simulation domain of models 2C20 and 3C20 against time, split into compressible, solenoidal and total part. Compressible motions dominate because of the inflows. *Right*: Specific kinetic energy for the cold gas ($T < 300\text{K}$) of models 2C20 and 3C20 against time, split into compressible solenoidal and total part. Solenoidal motions dominate in the cold gas.

sured” by the highly compressible inflow. Even the gas in the isothermal branch (i.e. gas which has cooled down to the minimum temperature) resides at pressures between the initial thermal equilibrium pressure and the ram pressure of the inflow (see also Vázquez-Semadeni et al. 2006 – an effect which traditionally has been assigned to self-gravity, e.g. Pringle et al. 2001). The more or less linear black regions at $\log n \approx -0.5$ are a result of the adiabatic reaction of the shock-compressed gas, i.e. this gas has had not yet time to react to thermal effects (see also Young & Mac Low 2006). The dashed red line denotes

the Hugoniot curve

$$\left(n_2 - \frac{\gamma - 1}{\gamma + 1}n_1\right) P_2 = \left(n_1 - \frac{\gamma - 1}{\gamma + 1}n_2\right) P_1, \quad (6)$$

that is, the pairs of values (P, n) for the state on one side (index 1) of the shock front that are compatible with the Rankine-Hugoniot jump conditions across (index 2) the shock front (Courant & Friedrichs 1948). This has also been noted by Audit & Hennebelle (2005).

From Figure 15 we see that the thermally unstable gas is generally still fast-moving, i.e. it has passed the bounding shocks but has not yet met the slab of dense, cold material (of course the initial inflow just shows up as a single dot in the $P(n)$ and $v(n)$ plots). High-density gas is mostly moving at a few km s^{-1} , consistent with the line-of-sight velocity dispersion discussed in §5.1.

A small fraction of cells (1.7×10^{-3} for model 2C20, and 1.9×10^{-4} for model 2C30) seems to exhibit velocities larger than the inflow velocity. This is hard to understand because there is no physical mechanism to accelerate gas to velocities higher than inflow velocities. All of those cells coincide with the largest density/temperature jumps occurring in the simulation and have slightly increased temperatures as well. Thus, they are a consequence of a slight overshoot from the reconstruction step in the scheme. Since the fraction of faulty cells does not vary over time (once the cold gas has formed), we simply neglect these cells for the analysis.

For our later discussion of critical masses for molecular cloud formation, Figure 16 summarizes the mass content in the three thermal regimes, defined by the warm stable range ($T > 3000\text{K}$), the cold stable range ($T < 300\text{K}$) and the instability range in between. Obviously, once the cold regions form, most of the gas is locked there. The amount grows linearly with time, indicating that although the PoMClOC is turbulent, it essentially acts like a slab for collecting cold material. The warm phase (center panel) contains a close to constant amount of mass with time – it is just a transitory phase in our models. At any given time only a small fraction (but still a few percent) of the total mass is passing through the unstable regime. This mass fraction depends slightly on the Mach number of the inflow, because the shorter dynamical time scales compete with the thermal time scales, so that gas which has been thrown out of thermal equilibrium will have less chance of attaining equilibrium conditions again. A similar effect can be seen in the temperature maps (Fig. 2): For lower Mach numbers, the transition from warm (yellow) to cold (blue) gas is much more pronounced (see also Sánchez-Salcedo et al. 2002 and Vázquez-Semadeni et al. 2006). Conversely, a high

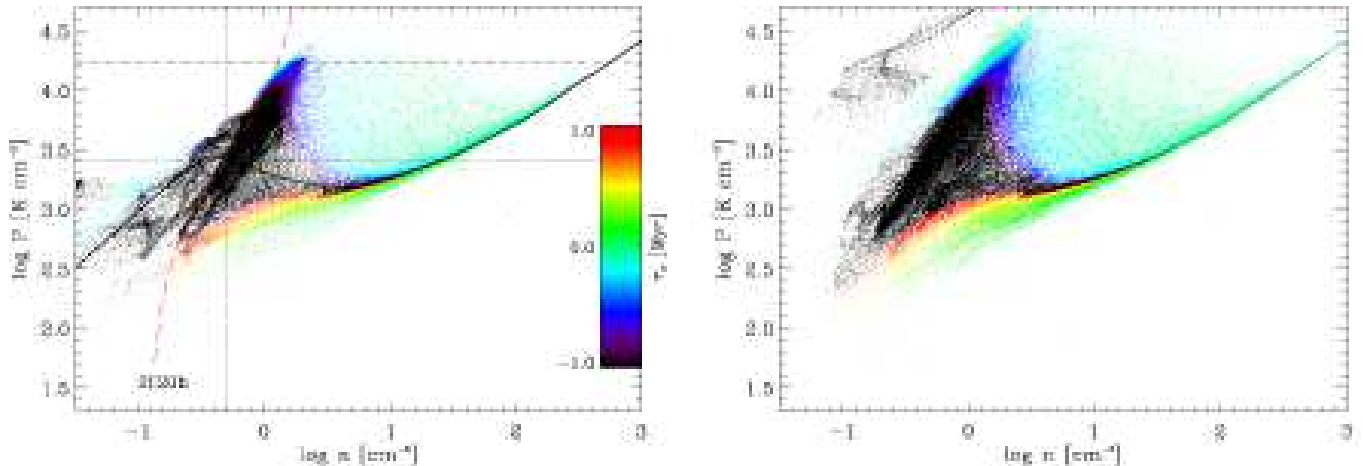


FIG. 14.— Scatterplot of pressure against density 12 Myrs after initial flow contact, color-coded with the thermal time scale τ_c (eq. 1), for models 2C20 and 2C30. Negative τ_c corresponds to cooling, positive τ_c to heating. The solid line denotes the equilibrium $P(n)$ -distribution, the dotted lines stand for the initial conditions, and the dashed (black) line corresponds to the ram pressure of the inflow, $p_r \equiv n v_0^2$. The dashed red line denotes the Hugoniot curve (eq. [6]).

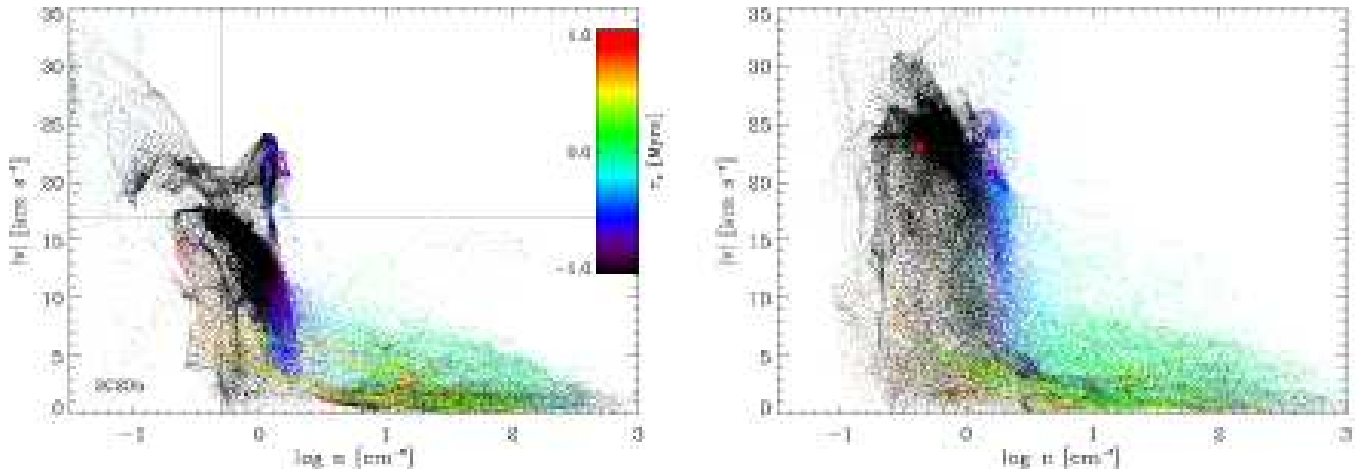


FIG. 15.— Scatterplot of absolute velocity against density 12 Myrs after initial flow contact, color-coded with the thermal time scale τ_c (eq. 1), for models 2C20 and 2C30. Negative τ_c corresponds to cooling, positive τ_c to heating. Dotted lines denote the initial conditions. The fast-moving gas is generally in the thermally unstable regime.

fraction of gas in the unstable regime (Heiles & Troland 2003) might indicate a highly dynamical environment. A similar effect exists for 3D versus 2D models: Since the compressible modes are stronger in the 2D case, gas tends to be forced to cool in compressions, while in the 3D case, it can evade the compression and cooling by shearing motions, which even would lead to additional heating. As Figure 16 shows, neither resolution nor geometry affects the mass fractions in the stable temperature regimes significantly. Especially, the fraction of mass in the cold phase (Fig. 16, left panel) is indistinguishable for models at resolution $N = 512$ and $N = 1024$.

5.3. Driving Efficiency

Comparing the kinetic energy of the inflow to that in the unstable and cold (see §5.2) gas phases allows us to estimate the efficiency of turbulent “driving” in our models, i.e. the efficiency with which the highly ordered kinetic energy of the inflow is converted to the turbulent motions within the PoMClOC. Figure 17 shows the ratio of the kinetic energy change to the energy input rate of

the inflow, the efficiency,

$$\mathcal{E} \equiv \frac{\partial_t \int n v^2 dV}{n_0 v_0^3 A}, \quad (7)$$

in the cold (filled symbols) and unstable (open symbols) gas. The integral extends over all cells within the chosen temperature regime, and A is the area of the inflow. Overall, the efficiency \mathcal{E} in the cold gas ranges between 2% and 5%. This is consistent with the ratio of the inflow speed to the line-of-sight velocity dispersion (see e.g. Fig. 9). In other words, most of the energy is lost due to atomic line cooling. Gas in the unstable phase reaches an efficiency which is smaller by a factor of ≈ 5 : an effect of the lower densities (the velocities are generally higher, see Fig 15). There seems to be a weak trend to smaller efficiency \mathcal{E} with larger energy inflow $n_0 v_0^3 A$: Larger inflow velocities result in higher compressions and thus in faster cooling, by which a growing fraction of the input energy is lost.

5.4. Conditions for H_2 Formation

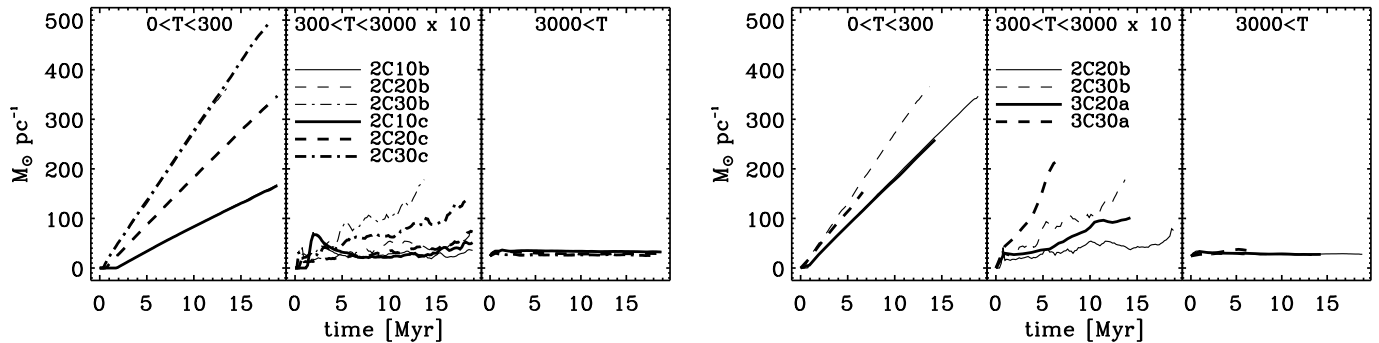


FIG. 16.— Mass content in the warm ($T > 3000\text{K}$), unstable ($300 < T < 3000\text{K}$) and cold ($T < 300\text{K}$) phase, for a resolution (left panel) and geometry (right panel) test. Note that in order to compare between 2D and 3D models, the mass content is given per length, i.e. the 3D models have been integrated along the z -direction. For convenience, the mass fraction in the unstable regime has been multiplied by 10.

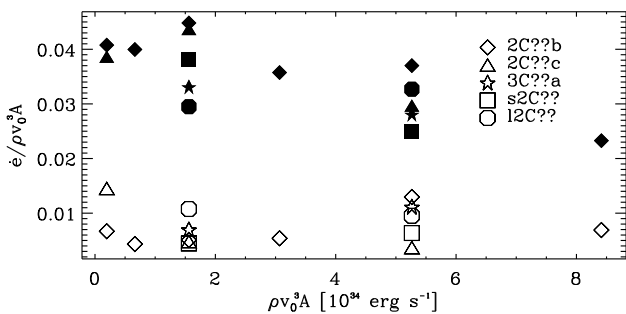


FIG. 17.— Ratio of kinetic energy change to energy input rate in the unstable (open symbols) and cold (filled symbols) gas phases (see expression 7) for the models indicated. Question marks in the model names are wild cards for the Mach numbers. Only a few percent of the energy input is transferred to the cold gas.

A crucial point in our analysis is whether the cold gas reaches conditions favorable for H_2 formation, and thus eventually for molecular clouds (so far we have only been talking about the precursors of molecular clouds). Three criteria need to be met.

(1) For H_2 formation, the gas temperature has to drop below a threshold temperature which we take to be $T_c = 300\text{K}$ (Cazaux et al. 2005). This might appear to be somewhat high, since the sticking probability decreases rapidly with higher temperatures, and is near unity only for $T < 20\text{K}$ (Cazaux & Tielens 2004; Bergin et al. 2004). Nevertheless, we chose the above temperature limit, because it turns out that once the temperature of a gas parcel has dropped below $T = 300\text{K}$, it will quickly cool down to the minimum temperature allowed by the cooling prescription. In that sense, the time scales give a lower limit, i.e. denote the point at which the first H_2 could potentially be formed. Since the cooling curve only extends down to 30K anyway, we cannot make more detailed statements about H_2 formation. From Figure 16 we already saw that for reasonable inflow speeds, a few $100M_{\odot} \text{ pc}^{-1}$ at $T < 300\text{K}$ accumulate within approximately 8 Myrs. This material would be in principle available for H_2 formation – at least as far as the temperature is concerned.

(2) The (now cold) gas has to stay cold “long” enough to allow for H_2 formation. Time estimates for H_2 formation vary. In their analysis of H_2 formation behind

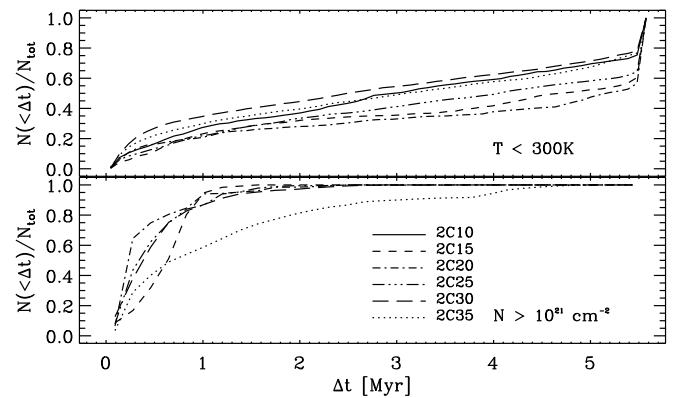


FIG. 18.— Cumulative histogram of time intervals over which tracer particles stay at temperatures $T < 300\text{K}$ (top), and over which tracer particles “see” column densities $N > 10^{21} \text{ cm}^{-2}$ with respect to the ambient UV radiation field (bottom). Model sequence in Mach number. Model 2C35 ended 6 Myrs after initial tracer deployment. All models were run at $N = 512$.

shock fronts, Bergin et al. (2004) quote time scales between 5 and 10 Myrs, depending on the inflow momentum. Once H_2 exists, its further formation could well be a run-away process, since self-shielding is much more efficient than dust shielding. This means that the critical time scale is given by the onset of H_2 formation. A minimum requirement therefore is that the cold gas is not re-heated during this time scale. To measure this, we followed the temperature history of the tracer particles and determined how long each particle stays cold. The top panel of Figure 18 is a cumulative histogram of the time intervals over which tracer particles have temperatures $T < 300\text{K}$. Apart from a small fraction at short time intervals ΔT (these are particles at the rims of the cold regions), most of the particles stay cold for at least 6 Myrs. In fact, for most models, the cold gas parcels stay cold for over 14 Myrs, i.e. once it has cooled down, by far most of the gas stays cold. Model 2C35 ended 6 Myrs after the initial tracer deployment, so in order to compare to the other models, all had to be evaluated to a maximum time interval of $\Delta t = 6$ Myrs, since otherwise it would look as if particles are re-heated in model 2C35 after 6 Myrs. To summarize the top panel of Figure 18, the gas stays cold long enough to allow for H_2 formation.

(3) Finally, the cold, dense gas could be re-exposed to

the ambient UV radiation field. H_2 formation requires a critical column density of $N(\text{HI}) \gtrsim 10^{21} \text{ cm}^{-2}$. This we can determine again with the tracer particles, resulting in the bottom panel of Figure 18, which combines the temperature criterion of the top panel and the column density threshold. Dropping the temperature criterion does not affect the result. Thus the critical quantity is the shielding column density, not the temperature. In other words, once the gas enters the “cold” phase, its thermal time scale is short compared to the dynamical time scale, so that the gas stays isothermal (see Fig. 14). However, due to the continuous re-structuring of the cloud, gas is repeatedly re-exposed to the UV radiation field and the column density of the cold gas only stays above 10^{21} cm^{-2} for about 1 Myr. This is a direct consequence of the PoMClOC’s highly dynamical nature. Note that Figure 18 gives a pessimistic view: once a small fraction of the particles has reached conditions beneficial for H_2 formation, self-shielding will set in. The analysis up to now only includes shielding by dust. The inflow velocity of model 2C10 is too low to reach sufficiently large column densities for H_2 formation in the elapsed time of the simulation. As Bergin et al. (2004) found in one dimension, average column densities must achieve values of 10^{21} cm^{-2} for H_2 formation to occur because of the shielding requirement.

6. A SUMMARY AND DISCUSSION

Molecular clouds in our Galaxy are complex and highly-structured, with broad, non-thermal line-widths suggesting substantial turbulent motions. Thus, molecular clouds very likely are not static entities and might not necessarily be in an equilibrium state, but their properties could well be determined by their formation process. We presented numerical models of the formation of precursors of molecular cloud complexes (PoMClOCs), in large-scale colliding HI-flows. We will now summarize our findings and discuss their astrophysical relevance.

6.1. Effects of Boundary Conditions

In §4 we discussed to what extent numerical artifacts might influence our conclusions. One last effect needs to be mentioned, namely the choice of the boundary conditions. While the boundary conditions in the horizontal direction are prescribed by the inflow, we are free to define the boundaries in the transverse direction. As mentioned in §4.4.2, our standard choice is periodic boundary conditions, i.e. material leaving the simulation domain at the bottom reenters at the top and vice versa (same holds for the tracer particles). This might raise the question of whether the level of turbulence and the amount of cold gas in the simulations is a “closed box” effect in the sense that if the boundaries were open the compressed gas could leave the simulation domain before cooling down and contributing to the cold gas mass.

In order to assess the effects of this specific boundary choice, we ran a set of models with open boundary conditions in the direction transverse to the inflow, i.e. gas is free to leave the simulation domain. Models s2C20 and s2C30 (Fig. 19, top) have the same box size as models 2C20 and 2C30 (Fig. 2), while in models l2C20 and l2C30, the simulation domain was enlarged in the transversal direction (Fig. 19, bottom) in such a way that the inflow region has the same size as in the

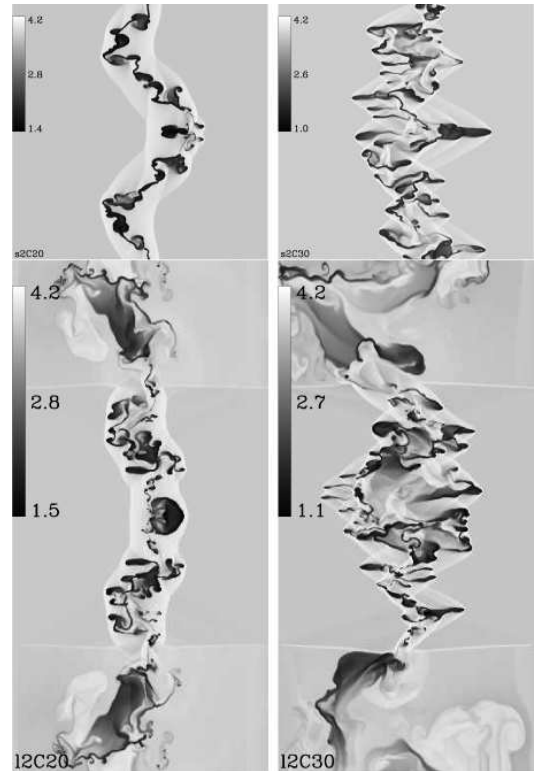


FIG. 19.— *Top*: Stills of models s2C20 and s2C30 with open boundary conditions in the transversal direction. The resolution is $N = 512$. *Bottom*: Stills of models l2C20 and l2C30 with open boundary conditions in the transversal direction and an “inactive” region above and below the inflow. The resolution is $N = 512 \times 1024$.

square models (e.g. 2C20, 2C30), but above and below this inflow region we place “inactive” regions into which the compressed gas can stream. In other words, not only are the boundaries in the transverse direction open, but there is no inflow in the x-direction in the “inactive” regions (in fact, they are open boundaries, i.e. material is free to leave the box).

The morphologies of models with open and periodic boundaries are slightly different, but not disquietingly so. For the non-periodic models, note that while there is a clear outflow observable in l2C20 and l2C30, its signature is weak in s2C20 and s2C30. The open boundaries are implemented via a constant extrapolation of the last active cells, so that the pressure gradient at the boundary in the transverse direction is constant. However because for models l2C20 and l2C30 we implement an “inactive” region above and below the inflow region, the gas in the dense compressed region, i.e. the inflow region, sees a pressure gradient along the transverse direction at the boundaries between the “active” and “inactive” regions.

For models l2C20 and l2C30, dense gas is definitely squeezed between the colliding flows out into the “inactive” regions. How does this affect the mass budget? Figure 20 shows the mass per length contained in the three temperature regimes as in Figure 16, but for models 2C20, s2C20 and l2C20.

Clearly, the total mass (i.e. the sum over the three temperature regimes) increases linearly, dominated by the growth of the cold mass fraction. Only model l2C20

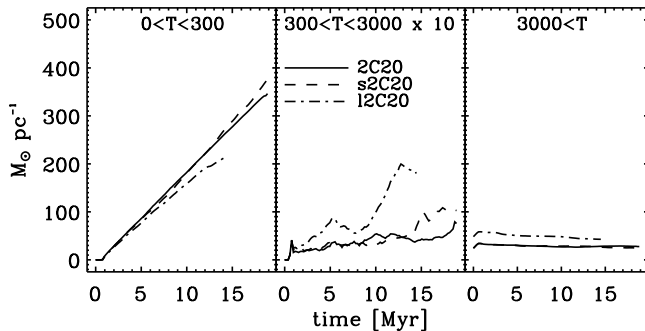


FIG. 20.— Mass content in the warm ($T > 3000\text{K}$), unstable ($300 < T < 3000\text{K}$) and cold ($T < 300\text{K}$) phase, for models 2C20, s2C20 and l2C20. For convenience, the mass fraction in the unstable regime has been multiplied by 10. The total mass in the simulation domain increases (more or less) linearly for all models, despite the open boundary conditions of models s2C20 and l2C20.

shows some deviation from a linear evolution at later times. The cooling time scale is much shorter than the flow time scale and the sound crossing time, so that the gas is compressed and cooled down before it can feel the boundaries. In other words, gas in the incoming flow cools efficiently, and structures within the slabs form independent of the boundary conditions. We conclude that our discussions of the mass budget and the level of turbulence are nearly independent of the specific boundary condition choice.

6.2. Turbulence

Observed line-of-sight velocity dispersions of a few km s^{-1} in the cold gas are reproduced by the models (Fig. 7). Yet, the *internal* velocity dispersions are generally subsonic, i.e. it seems as if the term “supersonic” is not necessarily an accurate description of the hydrodynamical state of the cold gas (Figs. 8 and 9). Hartmann (2002) argues, that because of the ages and small spatial dispersions of young stars in Taurus, their velocity dispersions relative to their natal gas are very likely subsonic. The turbulent line-widths amount only to a fraction of the inflow velocity.

The subsonic internal velocity dispersions come as a surprise, and the question arises whether self-gravity could lead to higher internal dispersions. While this is definitely something to test, to drive internal motions, gravity would have to act on local non-linear perturbations within the cold gas, for whose growth there simply might not be enough time available (Burkert & Hartmann 2004).

The above result would affect some aspects of the model of turbulence-controlled star formation (see Mac Low & Klessen 2004). There, supersonic turbulence leads to non-linear (isothermal) shock compressions which in turn trigger (at least partly) fragmentation and subsequent gravitational collapse. By this fragmentation mechanism star formation is “localized” in the sense that before the whole cloud can collapse, the non-linear density perturbations caused by supersonic turbulence have formed stars (see also Burkert & Hartmann 2004). In the absence of supersonic turbulence in the cold regions, the non-linear density perturbations must arise during the formation process of the cloud. These perturbations could be envisaged as the cold filaments which are a con-

sequence of the combination of dynamical and thermal instabilities. The subsonic internal motions are mirrored in the specific kinetic energy modes (Fig 13) and spectra (Fig. 12). They clearly point to weakly compressible turbulence in the cold gas.

Turbulence is generated with ease in the colliding flow scenario, and the resulting PoMClOC reproduces observational bulk quantities. One possible consequence of turbulence as an initial-condition effect is the efficient mixing between warm and cold phases in the complex. There is an ongoing debate about the degree of mixing between atomic and molecular hydrogen in MCCs. While there is no doubt about the intermittent density (and velocity) structure in molecular clouds, it is less clear, what the diffuse, possibly warmer medium is made out of. Turbulent mixing would point to CNM, i.e. HI, while H_2 self-shielding and H_2 formation time scale arguments would favor a fully molecular cloud. The “openings” in the clouds (no matter whether they are e.g. channels, gaps or holes) might play a crucial role for the internal dynamics of the clouds: Hennebelle & Inutsuka (2005) argue that the channels of warm material in MCCs allow energy (in their case in the form of Alfvén waves) to enter the cloud and thus to drive the internal motions. However, this would only refer to motions of the cold gas regions with respect to each other, but not necessarily to internal motions in the cold gas.

6.3. Thermal States

Because of its very short thermal time scales, the dense gas closely follows the thermal equilibrium relation between pressure and density (Fig. 14). This gas phase is approximately isothermal and corresponds to the dense, isolated regions which we identify as precursors of molecular gas.

A perceptible amount of gas resides in the thermally unstable phase, consistent with observations by Heiles & Troland (2003), also consistent with the modeling results of other groups (e.g. Dib & Burkert 2005; Vázquez-Semadeni et al. 2006). The thermally unstable gas generally travels at high velocities (Fig. 15), meaning that it corresponds to gas which has passed the bounding shock but has not yet “fallen onto” the cold, dense objects (where it would cool down to the isothermal cloud temperature). The amount of unstable gas varies with the inflow Mach number, which is a consequence of competing dynamical and thermal time scales.

6.4. Conditions for H_2 -Formation

Given a sufficiently high inflow speed, colliding flows are an efficient way to assemble enough cold gas to form molecular clouds. Despite the highly structured objects, the amount of cold mass increases approximately linearly with time as if collected in a cold slab (Fig. 16). Once the gas has cooled below $T \approx 300\text{K}$ in our models, it stays cold (Fig. 18): the cold material has very short thermal time scales, i.e. it is close to isothermal (in Fig. 14, $(d \log P)/(d \log n) \rightarrow 1$ for $n > 100 \text{ cm}^{-3}$).

The main limiting factor for H_2 formation in our models is not the temperature of the gas, but the highly time-dependent column density. Because of the dynamical nature of the clouds, gas is continuously re-exposed to the ambient radiation field. Most of the gas manages to stay above shielding column densities of $N > 10^{21} \text{ cm}^{-2}$ only

for 2Myrs at most (Fig. 18). However, these estimates are pessimistic: (a) We only considered extinction by dust, not self-shielding by already formed H_2 . (b) Molecular clouds might not form “from scratch”, i.e. only from HI. Instead, the inflows might already contain a substantial amount of H_2 (see e.g. Pringle et al. 2001). This not only would shift the mass budget in favor of H_2 , but also would provide efficient self-shielding early on in the molecular cloud formation process.

6.5. Cloud Formation Time Scales

Even more than 10Myrs after flow contact time, in all our runs the total mass collected in the cold gas falls short of typical molecular cloud masses by a factor of approximately 10. The average column density essentially evolves one-dimensionally, i.e. $N(t) = n v_0 t \approx 1 \times 10^{20} \text{cm}^{-2} (t/\text{Myr})$ for the fastest inflow speed in our models. Thus, at least 10 Myrs are needed to reach an *average* column density high enough for self-shielding (since the dynamics lead to local focusing of the gas flows, isolated regions might reach this stage earlier, but not markedly so, see Bergin et al. 2004). Two remedies come to mind: (1) The cold mass growth rate depends nearly linearly on the inflow momentum (Fig. 16). However, the observed velocities and densities in the Galactic HI limits the inflow momentum to approximately $n_0 v_0 < 30 \text{km s}^{-1} \text{cm}^{-3}$, or – equivalently – $n_0 v_0 t \approx 10^{21} \text{cm}^{-2}$. Thus, molecular clouds might preferentially form in flows where the ambient atomic density is higher than the average density, i.e. $n_0 = 3 \text{cm}^{-3}$, $v_0 = 10 \text{km s}^{-1}$. Then, the mechanism described above might well dominate the formation of low-mass molecular clouds. More massive objects need either more time or a different parameter regime as in e.g. galaxy mergers. (2) The models presented here do not account for gravity. Since a slab-like geometry is favored by construction in the colliding flow scenario, gravity would lead to collapse in the plane, causing the densities (and column densities) needed for shielding to be rapidly reached. In that sense, any time scales given for conditions favorable for H_2 formation are upper estimates. Note that the *lateral* collapse can set in much later, and, if the cloud is large enough, and sufficiently dense substructures exist, might only occur after stars have formed locally.

We would like to stress the point that since the presented models are concerned with the formation of precursors of molecular clouds, the somewhat largish assembly time scales do not constitute a problem for short molecular cloud lifetimes. As Bergin et al. (2004) discussed, the ratio of the precursor’s assembly time scale over the actual molecular cloud lifetime can be as large as the relative amounts of atomic over molecular gas (approximately a factor of 4 in the solar neighborhood, Dame 1993; Savage et al. 1977). For a molecular cloud life time of, say, 3Myrs in the solar neighborhood (Hartmann et al. 2001 and references therein), the accumulation time for the PoMCloC would be expected to range around $\gtrsim 10$ Myrs. Obviously, the *molecular cloud* lifetime starts only once molecules are being formed.

Our models generally run longer than 10 Myrs. At an inflow velocity of 10km s^{-1} , this corresponds to a coherent flow of approximately 100pc, or strictly speaking, twice that length for a colliding flow. Although higher flow velocities and/or densities (note that at least with

the densities we seem to be on the lower side of the parameter range, see e.g. Bergin et al. 2004) would allow shorter time scales and thus shorter coherence lengths, the question nevertheless arises whether such coherent flows are realistic. On smaller scales (and higher densities), the interaction of winds of nearby stars might provide a possible source (see e.g. Churchwell et al. 2004), while on larger scales, the most probable source would be interacting supernova shells. The somewhat longish assembly timescales suggest that the initial densities of the flows are more likely to be a few cm^{-3} to form molecular clouds with flows of order 50-100 pc length. Spiral density waves can also produce coherent flows of the required length, at least in principle.

7. FUTURE WORK

The main purpose of this work was to demonstrate that precursors of molecular cloud complexes forming in colliding flows reproduce observational measures such as line-widths and column densities, without any recourse to initially imposed perturbations. The combination of dynamical and thermal instabilities efficiently generates the non-linear substructures necessary for a fast gravitational collapse and a (close to) instantaneous onset of star formation, thus meeting the short time scales required by observations (e.g. Hartmann 2003). Once the material is cold and dense, it seems difficult to drive highly supersonic motions (unless there is an internal driver, meaning stars) (Vasquez 1990; Balsara 1996, see however Miesch & Zweibel 1994) or even to mix it with warm gas (Heitsch et al. 2006). However, the cold and warm gas must be efficiently mixed in order to allow the cold material to move “freely” at velocities which are supersonic with respect to the cold gas’ temperature. Thus, the cold substructures must arise during the formation process of the cloud, from compression and cooling in the warm phase. We demonstrated that colliding flows provide a generic physical mechanism for creating non-linear structure in PoMCloCs, without any recourse to perturbed initial conditions. In their further evolution (i.e. beyond the models presented here), these non-linear perturbations will be the seeds for gravitational collapse and star formation. Thus, our models show that – from a dynamical point of view – the concept of “short” cloud life times is feasible. Ultimately, one can begin to see how realistic the concept of “turbulent support” of molecular clouds actually is (see e.g. Ballesteros-Paredes et al. 1999).

An MCC in the solar neighborhood has an average column density of $N(\text{HI}) \approx 1.4 \times 10^{21} \text{cm}^{-2}$ (McKee 1999), coinciding with the dust-shielding column density necessary for H_2 formation. Once this value is reached, H_2 -formation is expected to begin. Within 2 or 3 more Myrs, star formation will have occurred, and the cloud will have dispersed again. Within this scenario, the average column density of an ensemble of MCCs should be roughly constant, implying a mass-size relation of $M \propto L^2$. The latter would be expected for a Larson (1981) relation of the type $\sigma \propto L^{2/5}$, consistent with observed scalings (e.g. Elmegreen & Scalo 2004).

Clearly, this study leaves us with many unanswered questions. Gravity might lead to global edge effects (Burkert & Hartmann 2004) as well as to local “supersonic” velocities and to additional instabilities (see e.g.

Hunter et al. 1997; Hueckstaedt et al. 2005). Actual H₂ formation would further lower the temperature in the cold gas, in which case eventually supersonic velocities might be reached. The inflows might already be partially molecular, in which case the filling factor of H₂ should be low (Pringle et al. 2001). And finally, magnetic fields could influence and maybe control the structure formation (e.g. Vázquez-Semadeni et al. 1995; Passot et al. 1995; Elmegreen 1999; Hartmann et al. 2001).

We thoroughly enjoyed the discussions with J. Gal-

agher, K. Menten, L. Sparke, J. Stutzki and E. Zweibel, and we thank the anonymous referee for a critical and constructive report. Computations were performed on Ariadne built and maintained by S. Jansen at UW-Madison, at the NCSA (AST040026), and on the SGI-Altix at the USM, built and maintained by M. Wetzelstein and R. Gabler. This work was supported by the NSF (AST-0328821) and has made use of NASA's Astrophysics Data System.

REFERENCES

- Audit, E., Hennebelle, P. 2005, *A&A*, 433, 1
 de Avillez, M. A., & Breitschwerdt, D. 2005, *A&A*, 436, 585
 Ballesteros-Paredes, J., Hartmann, L., Vázquez-Semadeni, E. 1999, *ApJ*, 527, 285
 Ballesteros-Paredes, J., Vázquez-Semadeni, E., & Scalo, J. 1999, *ApJ*, 515, 286
 Bally, J., Stark, A. A., Wilson, R. W., & Langer, W. D. 1987, *ApJ*, 312, L45
 Balsara, D. S. 1996, *ApJ*, 465, 775
 Bergin, E. A., Hartmann, L. W., Raymond, J. C., Ballesteros-Paredes, J. 2004, *ApJ*, 612, 921
 Blondin, J. M., Marks, B. S. 1996, *New Ast.*, 1, 235
 Burkert, A., Hartmann, L. 2004, *ApJ*, 616, 288
 Burkert, A., Lin, D. N. C. 2000, *ApJ*, 537, 270
 Burkert, A., & Heitsch, F. 2006, *in preparation*
 Cazaux, S., & Tielens, A. G. G. M. 2004, *ApJ*, 604, 222
 Cazaux, S., Caselli, P., Tielens, A. G. G. M., Le Bourlot, J., Walmsley, M. 2005, *J. Phys.*, 6, 155
 Chandrasekhar, S. 1961, *International Series of Monographs on Physics*, Oxford: Clarendon, 1961,
 Churchwell, E., et al. 2004, *ApJS*, 154, 322
 Courant, R., & Friedrichs, K. O. 1948, *Supersonic Flow and Shock Waves*; Interscience Publishers, New York
 Dame, T. M. 1993, *AIP Conf. Proc.* 278: Back to the Galaxy, 278, 267
 Dib, S., & Burkert, A. 2005, *ApJ*, 630, 238
 Elmegreen, B. G. 1993, *ApJ*, 419, L29
 Elmegreen, B. G. 1999, *ApJ*, 527, 266
 Elmegreen, B. G. 2000, *ApJ*, 530, 277
 Elmegreen, B. G., Scalo, J. 2004, *ARAA*, 42, 211
 Falgarone, E. 1990, *Liege International Astrophysical Colloquia*, 29, 173
 Falgarone, E., Phillips, T. G. 1990, *ApJ*, 359, 344
 Falgarone, E., & Phillips, T. G. 1996, *ApJ*, 472, 191
 Ferrari, A., & Trussoni, E. 1983, *MNRAS*, 205, 515
 Field, G. B. 1965, *ApJ*, 142, 531
 Gerwin, R. A. 1968, *Rev. Mod. Phys.*, 40, 652
 Hartmann, L., Ballesteros-Paredes, J., Bergin, E. A. 2001, *ApJ*, 562, 852
 Hartmann, L. 2002, *ApJ*, 578, 914
 Hartmann, L. 2003, *ApJ*, 585, 398
 Heiles, C. 2004, *ASP Conf. Ser.* 323: Star Formation in the Interstellar Medium: In Honor of David Hollenbach, 323, 79
 Heiles, C., & Troland, T. H. 2003, *ApJ*, 586, 1067
 Heitsch, F., Zweibel, E. G., Slyz, A. D., & Devriendt, J. E. G. 2004, *ApJ*, 603, 165
 Heitsch, F., Burkert, A., Hartmann, L., Slyz, A. D., Devriendt, J. E. G. 2005, *ApJ*, 633, L113
 Heitsch, F., Slyz, A. D., Devriendt, J. E. G., Burkert, A. 2006, *in preparation*
 Hennebelle, P., Pérault, M. 1999, *A&A*, 351, 309
 Hennebelle, P., Pérault, M. 2000, *A&A*, 359, 1124
 Hennebelle, P., Whitworth, A. P., Gladwin, P. P., & André, P. 2003, *MNRAS*, 340, 870
 Hennebelle, P., Whitworth, A. P., Cha, S.-H., & Goodwin, S. P. 2004, *MNRAS*, 348, 687
 Hennebelle, P., & Inutsuka, S. 2005, *astro-ph/0510389*
 Hueckstaedt, R. M. 2003, *New Ast.*, 8, 295
 Hueckstaedt, R. M., Peterson, A. H., & Hunter, J. H. 2005, *MNRAS*, 361, L35
 Hunter, J. H. 1979, *ApJ*, 233, 946
 Hunter, J. H., & Fleck, R. C. 1982, *ApJ*, 256, 505
 Hunter Jr., J. H., Sandford II, M. T., Whitaker, R., Klein, R.I. 1986, *ApJ*, 305, 309
 Hunter, J. H., Whitaker, R. W., & Lovelace, R. V. E. 1997, *ApJ*, 482, 852
 Keppens, R., Tóth, G., Westermann, R. H. J., Goedbloed, J. P. 1999, *J. Plas. Phys.*, 61, 1
 Klein, R. I., Woods, D. T. 1998, *ApJ*, 497, 777
 Koyama, H., & Inutsuka, S. 2002, *ApJ*, 532, 980
 Koyama, H., & Inutsuka, S. 2002, *ApJ*, 564, L97
 Koyama, H., & Inutsuka, S. 2004, *ApJ*, 602, L25
 Koyama, H., & Inutsuka, S. 2004, *RMxAC*, 22, 26
 Kritsuk, A. G., & Norman, M. L. 2002, *ApJ*, 569, L127
 Kritsuk, A. G., & Norman, M. L. 2002, *ApJ*, 580, L51
 Kritsuk, A. G., & Norman, M. L. 2004, *ApJ*, 601, L55
 Kwan, J., & Sanders, D. B. 1986, *ApJ*, 309, 783
 Larson, R. B. 1981, *MNRAS*, 194, 809
 Lis, D. C., Pety, J., Phillips, T. G., & Falgarone, E. 1996, *ApJ*, 463, 623
 Looney, L. W., Wang, S., Hamidouche, M., Safier, P. N., & Klein, R. 2006, *astro-ph/0601437*
 Mac Low, M.-M. 2004, *Ap&SS*, 289, 323
 Mac Low, M.-M., & Klessen, R. S. 2004, *Reviews of Modern Physics*, 76, 125
 Mac Low, M.-M., Balsara, D. S., Kim, J., & de Avillez, M. A. 2005, *ApJ*, 626, 864
 Malagoli, A., Bodo, G., & Rosner, R. 1996, *ApJ*, 456, 708
 McKee, C. F. 1999, *NATO ASIC Proc.* 540: The Origin of Stars and Planetary Systems, 29
 Miesch, M. S., & Zweibel, E. G. 1994, *ApJ*, 432, 622
 Mizuno, A., Onishi, T., Yonekura, Y., Nagahama, T., Ogawa, H., & Fukui, Y. 1995, *ApJ*, 445, L161
 Parker, E. N. 1953, *ApJ*, 117, 431
 Passot, T., Vázquez-Semadeni, E., & Pouquet, A. 1995, *ApJ*, 455, 536
 Priest, E. R., & Heyvaerts, J. 1974, *Sol. Phys.*, 36, 433
 Pringle, J. E., Allen, R. J., & Lubow, S. H. 2001, *MNRAS*, 327, 663
 Prendergast, K. H., Xu, K. 1993, *J. Comp. Phys.*, 109, 53
 Roberts, B. 1974, *Phys. Fluids*, 17, 1771
 Sandham, N. D., & Reynolds, W. C. 1991, *Journal of Fluid Mechanics*, 224, 133
 Sánchez-Salcedo, F. J., Vázquez-Semadeni, E., & Gazol, A. 2002, *ApJ*, 577, 768
 Savage, B. D., Bohlin, R. C., Drake, J. F., & Budich, W. 1977, *ApJ*, 216, 291
 Sen, A. K. 1964, *Phys. Fluids*, 7, 1293
 Slyz, A. D., Prendergast, K. H. 1999, *A&AS*, 139, 199
 Slyz, A. D., Devriendt, J. E. G., Bryan, G., & Silk, J. 2005, *MNRAS*, 356, 737
 Slyz, A. D., Devriendt, J. E. G., Bryan, G., Heitsch, F. & Silk, J. 2005, *MNRAS*, *submitted*
 Stutzki, J., & Güsten, R. 1990, *ApJ*, 356, 513
 Tohline, J. E., Bodenheimer, P. H., & Christodoulou, D. M. 1987, *ApJ*, 322, 787
 Vasquez, B. J. 1990, *ApJ*, 356, 693
 Vázquez-Semadeni, E., Passot, T., & Pouquet, A. 1995, *ApJ*, 441, 702
 Vázquez-Semadeni, E., Ryu, D., Passot, T., González, R. F., Gazol, A. 2006, *ApJ*, *accepted*
 Vishniac, E. T. 1994, *ApJ*, 428, 186

- Walder, R., Folini, D. 1998, ApSS, 260, 215
Walder, R., Folini, D. 2000, ApSS, 274, 343
Williams, J. P., Blitz, L., & Stark, A. A. 1995, ApJ, 451, 252
Williams, J. P., Blitz, L., & McKee, C. F. 2000, Protostars and Planets IV, 97
Wolfire, M. G., Hollenbach, D., McKee, C. F., Tielens, A. G. G. M., Bakes, E. L. O. 1995, ApJ, 443, 152
Young, M. K. R., & Mac Low, M.-M. 2006, astro-ph/0601005